

Generative Neural Network Channel Modeling for Millimeter-Wave UAV Communication

William Xia, *Student Member, IEEE*, Sundeep Rangan, *Fellow, IEEE*, Marco Mezzavilla, *Senior Member, IEEE*, Angel Lozano, *Fellow, IEEE*, Giovanni Geraci, *Senior Member, IEEE*, Vasilii Semkin, and Giuseppe Loianno, *Member, IEEE*

Abstract—The millimeter wave bands are being increasingly considered for wireless communication to unmanned aerial vehicles (UAVs). Critical to this undertaking are statistical channel models that describe the distribution of constituent parameters in scenarios of interest. This paper presents a general modeling methodology based on data-training a generative neural network. The proposed generative model has a two-stage structure that first predicts the state of the link (line-of-sight, non-line-of-sight, or outage), and subsequently feeds this state into a conditional variational autoencoder that generates the path losses, delays, and angles of arrival and departure for all the propagation paths. Importantly, minimal prior assumptions are made, enabling the model to capture complex relationships within the data. The methodology is demonstrated for 28 GHz air-to-ground channels between UAVs and a cellular system in representative urban environments, with training datasets produced through ray tracing. The demonstration extends to both terrestrial base stations (mounted at street-level) and aerial base stations (installed on rooftops).

Index Terms—UAV, drones, mmWave communication, 5G, 6G, cellular networks, air to ground, channel model, ray tracing, variational autoencoder, generative neural networks.

I. INTRODUCTION

Communication with unmanned aerial vehicles (UAVs) is a subject of growing interest, and the millimeter wave (mmWave) range is an inviting realm for this purpose because of the enormous bandwidth availability and the possibility of line-of-sight (LOS) transmissions [2]–[11]. As with any other communication system, the design and evaluation of mmWave UAV networks hinges crucially on the availability of suitable channel models, yet the current standard-defined air-to-ground channel model is only calibrated at sub-6 GHz frequencies [12]. Steps have been taken to cover this gap, e.g., in [13], which proposes a propagation model for UAV-to-UAV communication at 60 GHz, in LOS conditions, and with UAV altitudes ranging between 6 and 15 m. While this and other contributions are decidedly welcome, there is great interest

in more general models for UAV communication at mmWave frequencies.

Channel models have evolved over time and they have come to adopt, as their preferred form, that of parametric statistical descriptions: distributions are provided for the angles of arrival and departure, the gains, and the delays of multipath components; by sampling these distributions, the channel response at any time/frequency/location can be realized. The distribution of the path parameters (angles, gains, delays) must be distilled from a combination of physical considerations and field measurements [14], [15], a process that has become increasingly cumbersome as the systems being modelled have grown in complexity and heterogeneity (new frequency bands, broader bandwidths, massive antenna arrays, diverse deployments) [16]. In aerial settings, this complexity is further compounded by new parameter dependencies on the UAV altitudes, their 3D orientation, or the building heights, among others [12], [17]–[20]. Altogether, the parameters are bound to exhibit decidedly complex relationships that are very difficult to establish through analytical or physical considerations; this makes the modeling process utterly challenging and necessarily based, almost solely, on empirical data.

Once it is accepted that the parameter distributions need to emanate from empirical data, with minimal room for other considerations, data-driven machine-learning methods become an attractive recourse. Indeed, these methods entail minimal assumptions and can naturally capture intricate probabilistic relationships. Neural networks (NNs) have been specifically advocated in [21]–[25] for indoor mmWave channel modeling, whereby upon an input corresponding to some location, the NN outputs the model parameters for that location; in essence, the parameters are then a regression from the training dataset, much as in data-based signal power maps and in learning-based planning and prediction tools [26]–[33]. A strong aspect of all these works is their inherent site-specific nature, a virtue when it comes to optimizing specific deployments. Alternatively, there is interest in models that can produce channel parameters broadly representative of some general environment, say an urban microcellular system.

Generative NNs, which have proven enormously successful with images and text [34]–[36], offer a natural approach to data-driven channel modeling that can broadly represent complex settings, and some early works have successfully trialed generative adversarial networks (GANs) for simple wireless channels [37]–[39]. The present paper propounds a different generative NN structure, powerful and widely applicable, for

W. Xia, S. Rangan, M. Mezzavilla, and G. Loianno are with NYU Tandon School of Engineering, Brooklyn, USA. Their work is supported by NSF grants 1302336, 1564142, 1547332, and 1824434, NIST, SRC, and the industrial affiliates of NYU WIRELESS.

A. Lozano and G. Geraci are with Univ. Pompeu Fabra, Barcelona. Their work is supported by ERC grant 694974, by MINECO's Project RTI2018-101040, by ICREA, and by the Junior Leader Fellowship Program from "la Caixa" Banking Foundation.

V. Semkin is with VTT Technical Research Centre of Finland Ltd, Finland. His work is supported in part by the Academy of Finland.

Some of the material in this paper was presented at the 2020 IEEE GLOBECOM conference [1].

aerial channel modeling. For data provisioning, we rely on ray tracing (specifically the tool [40]), which has developed substantially for mmWave communication [41]–[46] and can supply datasets of the size required to train large NNs.

Ray tracing requires a detailed blueprint of the environment, including the size, shape, and location of all obstacles, along with their electromagnetic properties. And, as it employs high-frequency approximations, it exhibits some inaccuracies. Nonetheless, ray tracing is perfectly adequate for our purpose here, which is to validate the proposed methodology. We hasten to emphasize that, ultimately, the model is meant to be driven by field data, gathered either through targeted measurement campaigns or directly supplied by users of the service.

The highlights of this work are as follows:

- *Double-directional wideband channel modeling:* As chief point, we demonstrate that the proposed method can capture the directional characteristics of the channel at both transmitter and receiver along with its wideband nature, meaning the angular, gain, and delay information for all paths on each link. This description is compatible with 3GPP evaluation methodologies [12], [17] and can provide the full wideband MIMO response given specific antenna configurations at transmitter and receiver. No prior assumptions are made regarding the dependencies among parameters, and the model is able to capture relationships that are nuanced and interesting.
- *Novel NN structure:* The generative model features a novel two-stage structure where a first NN determines if the link is in a state of line-of-sight (LOS), non-line-of-sight (NLOS), or outage, while a second stage employs a conditional variational autoencoder (VAE) to predict the path parameters given that state. Importantly, several pre-processing steps are introduced to map the path parameters to a format compatible with NN outputs.
- *Application to UAV mmWave channel modeling:* The methodology is demonstrated by characterizing 28 GHz channels connecting UAVs with ground receivers; both street-level and rooftop-mounted receivers are considered.
- *Intra- and inter-environment generalization:* The model is separately trained on data from two environments, namely (i) an environment featuring high-rise buildings as well as wide open areas, embodied by sections of Tokyo and Beijing, and (ii) an environment dominated by low-rise buildings, represented by sections of London and Moscow. This allows testing the ability of the model trained in one environment to predict the behavior in new locations within that environment (intra-environment generalization) and in locations in the other environment (inter-environment generalization). Interestingly, the link state distribution is seen to vary substantially across environments, while the path parameters conditioned on that state generalize well.
- *Publicly available model:* The generative model developed in this work is publicly available [47] and can be readily incorporated to any simulator of mmWave UAV communication. And, beyond this use case, the underlying modeling framework may be enticing for other emerging communication scenarios such as terahertz systems, and even as an

alternative to traditional models in other contexts.

II. PROBLEM FORMULATION

We consider the modeling of channels linking a single transmitter with a single receiver. The UAV is taken to be the transmitter and the base station—gNB in 3GPP terminology [12]—the receiver, yet, owing to reciprocity, the roles of transmitter and receiver are interchangeable. Each link is described by the collection of parameters [48]

$$\mathbf{x} = \left\{ (L_k, \phi_k^{\text{rx}}, \theta_k^{\text{rx}}, \phi_k^{\text{tx}}, \theta_k^{\text{tx}}, \tau_k), k = 1, \dots, K \right\}, \quad (1)$$

where K is the number of paths whereas L_k is the loss of path k , $(\phi_k^{\text{rx}}, \theta_k^{\text{rx}})$ are its azimuth and elevation angles of arrival, $(\phi_k^{\text{tx}}, \theta_k^{\text{tx}})$ are its azimuth and elevation angles of departure, and τ_k is its absolute propagation delay. Unlike standard 3GPP spatial cluster models (e.g. [17]), we do not consider angular or delay dispersion within each path. This is not a limitation of the model, but only a consequence of the tool that produces the training datasets not accommodating diffuse reflections. If angular or delay spread information were available, these aspects could be included as well.

The number of paths is fixed at $K = 20$, with $L_k = L_{\max}$ for paths that are not actually present; we set $L_{\max} = 200$ dB, which is compatible with the maximum path loss detectable by the ray tracer. With these settings, the data vector \mathbf{x} in (1) contains $6K = 120$ parameters per link. Let

$$\mathbf{u} = (\mathbf{d}, c) \quad (2)$$

denote the *link condition*, with $\mathbf{d} = (d_x, d_y, d_z)$ the vector connecting the UAV with the gNB and with c indicating the type of gNB. Two types of gNBs are considered herein, specifically terrestrial street-level gNBs and aerial roof-mounted gNBs, but further types could be introduced as desired.

The goal is to capture the conditional distribution $p(\mathbf{x}|\mathbf{u})$, that is, to model the distribution of the paths in a link as a function of that link's condition in some environment. As anticipated, we consider a generative scheme in which as

$$\mathbf{x} = g(\mathbf{u}, \mathbf{z}), \quad (3)$$

where \mathbf{z} is a random vector, termed the *latent vector*, with some fixed prior distribution $p(\mathbf{z})$, while $g(\mathbf{u}, \mathbf{z})$ is the *generating function*, to be trained from data.

Once trained, generative models are conveniently applicable in simulations: the locations of UAVs and gNBs are determined, either deterministically or stochastically according to some deployment model, providing the condition vector \mathbf{u} for each link. Random vectors \mathbf{z} can then be produced for each link from the prior $p(\mathbf{z})$ and, from \mathbf{u} and \mathbf{z} , the path parameters \mathbf{x} follow as per (3). These parameters can be generated for both intended and interfering links and, in conjunction with the antenna patterns, array configuration, and beam tracking methods, they allow computing quantities of interest such as SNRs, SINRs, or bit rates.

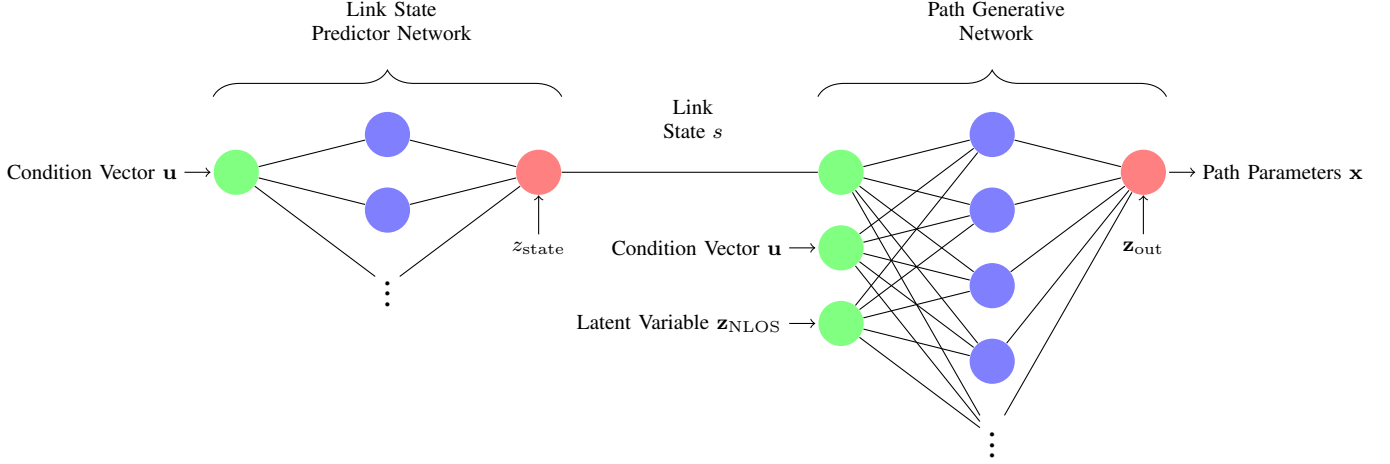


Fig. 1: Overall architecture for the two-stage generative model. The path generative network accepts a link condition vector \mathbf{u} and a latent vector $\mathbf{z} = (z_{\text{state}}, \mathbf{z}_{\text{NLOS}}, \mathbf{z}_{\text{out}})$ to generate random path parameters \mathbf{x} . For the sake of simplicity, various transformations, described in the text, have been omitted from the diagram.

TABLE I: Generative model configuration

	Link state prediction	Path VAE encoder	Path VAE decoder
Number of inputs	5	5 + 120	5 + 20
Hidden units	[25, 10]	[200, 80]	[80, 200]
Number of outputs	3	20 + 20	120 + 120
Optimizer	Adam	Adam	Adam
Learning rate	10^{-3}	10^{-4}	10^{-4}
Epochs	50	10000	10000
Batch size	100	100	100
Number of parameters	1653	44520	40720

III. PROPOSED GENERATIVE MODEL

A. Overview

The propounded generative model, depicted in Fig. 1, constructs the generative function as two cascaded NNs, namely a link-state prediction network followed by a path generative network. The latent vector \mathbf{z} subsumes three components,

$$\mathbf{z} = (z_{\text{state}}, \mathbf{z}_{\text{NLOS}}, \mathbf{z}_{\text{out}}). \quad (4)$$

The link-state prediction network accepts the condition vector \mathbf{u} and a random variable z_{state} , from which it determines the link state s . From s and the two other latent components, \mathbf{z}_{NLOS} and \mathbf{z}_{out} , the path generative network then produces the final path parameters \mathbf{x} . We next describe the details of this whole architecture.

B. Link-State Predictor Network

As recognized by standard 3GPP models such as [17], it is crucial to first determine the existence or lack of the LOS path. To this end, the link-state predictor accepts the condition vector \mathbf{u} defined in (2) and produces probabilities for the link being in one of three states [49]:

- **LOS**: The LOS path is present, possibly in addition to NLOS paths;
- **NLOS**: The LOS path is blocked, but at least one NLOS path is active;

- **NoLink**: No propagation paths (either LOS or NLOS) exist for this link.

In the sequel, $s \in \{\text{LOS}, \text{NLOS}, \text{NoLink}\}$ denotes the predicted link state while the generative model mapping \mathbf{u} to s is represented by

$$s = g_{\text{state}}(\mathbf{u}, \mathbf{z}_{\text{state}}). \quad (5)$$

Such mapping entails three steps, expounded next.

1) *Condition vector transformation*: The vector \mathbf{u} is transformed to the new vector,

$$(c_{\text{one}}, d_{3D} \mathbb{1}_{\{c=1\}}, d_z \mathbb{1}_{\{c=1\}}, \dots, d_{3D} \mathbb{1}_{\{c=C\}}, d_z \mathbb{1}_{\{c=C\}}), \quad (6)$$

where c_{one} is a one-hot coded version of the gNB type c while d_z is the vertical distance,

$$d_{3D} = \sqrt{d_x^2 + d_y^2 + d_z^2} \quad (7)$$

is the 3D distance, C is the number of possible gNB types, and $\mathbb{1}_{\{c=i\}}$ is the indicator function for the event $c = i$. As c can take C possible values, we can one-hot code c_{one} with $C - 1$ dimensions. Hence, the transformed vector in (6) has dimension $C - 1 + 2C = 3C - 1$. With $C = 2$ (terrestrial and aerial), the transformed vector in (6) has $3C - 1 = 5$ components. The motivation for the transformation in (6) is to enable a different behavior of the first layer of the NN for different types of gNB.

The transformed vector in (6) is passed through a min-max scaler that maps its components to values between 0 and 1; the limits on this min-max scaler are learned during training. The resulting transformed and scaled value is denoted by $\mathbf{v}_{\text{state}}$.

2) *NN*: A fully connected NN, configured as per Table I, generates the link state probabilities. The input to this NN is $\mathbf{v}_{\text{state}}$ while its output is a three-way softmax corresponding to the three states.

3) *Sampling*: In the final step, a uniform random variable $z_{\text{state}} \in [0, 1]$ samples the link state s based on the probability outputs from the NN.

C. Path Generative Network

This second stage generates the parameters \mathbf{x} in (1) given \mathbf{u} and s . This path generation also entails various steps, as described next.

1) *Condition vector transformation*: Again, we begin by transforming \mathbf{u} and s . For the path generative network, we propose the transformation,

$$(c_{\text{one}}, d_{3D}, 10 \log_{10}(d_{3D}), d_z, s), \quad (8)$$

where c_{one} , d_{3D} and d_z are as in (6). This five-dimensional vector is then passed through a min-max scaler to produce a five-dimensional vector with values from 0 to 1. We denote this transformed vector by \mathbf{v}_{path} .

2) *NLOS VAE model*: The next, and most intricate step, is to generate the parameters for the NLOS components within \mathbf{x} . As explained below, these NLOS components are represented in a transformed version denoted by \mathbf{y}_{NLOS} . For now, we note that there are up to $K = 20$ NLOS paths with 6 parameters per path, meaning that \mathbf{y}_{NLOS} is of dimension $6K = 120$.

The objective is to generate \mathbf{y}_{NLOS} from \mathbf{v}_{path} and from some randomness. This mapping should be trained such that the conditional distribution of \mathbf{y}_{NLOS} given \mathbf{v}_{path} matches the distribution in the training dataset. There are a large number of methods for training generative models, the two most common being variants of GANs [34], [35] or VAEs [36]. We found the most success with a VAE, as it avoids the minimax optimization required by a GAN.

We apply a standard architecture for the conditional VAE [36], that has itself two stages: A first stage inputs a random vector \mathbf{z}_{NLOS} along with \mathbf{v}_{path} and outputs means and variances for the NLOS components, namely

$$[\boldsymbol{\mu}, \boldsymbol{\sigma}^2] = g_{\text{NLOS}}(\mathbf{v}_{\text{path}}, \mathbf{z}_{\text{NLOS}}). \quad (9)$$

The vectors $\boldsymbol{\mu}$ and $\boldsymbol{\sigma}^2$ share the dimensions of the sought \mathbf{y}_{NLOS} , hence they combine into 120+120 output values. The entries of \mathbf{z}_{NLOS} are i.i.d. Gaussian with mean zero and unit variance. In VAE terminology, the dimension of \mathbf{z}_{NLOS} is called the *latent dimension*, with higher such dimensions enabling better fitting to the data but requiring larger training datasets. In the remainder, the latent dimension is fixed at 20.

The sought \mathbf{y}_{NLOS} is sampled from the means and variances,

$$\mathbf{y}_{\text{NLOS}} = \boldsymbol{\mu} + \boldsymbol{\sigma} \odot \mathbf{z}_{\text{out}}, \quad (10)$$

where \mathbf{z}_{out} has zero-mean unit-variance i.i.d. Gaussian entries and \odot indicates entry-wise multiplication.

In the VAE paradigm, the generator in (9) is termed the *decoder*. The VAE also requires training a so-called *encoder* that maps data samples \mathbf{y}_{NLOS} , \mathbf{v}_{path} back to the latent vector \mathbf{z}_{NLOS} . This encoder attempts to approximate sampling from the posterior density of \mathbf{z}_{NLOS} given \mathbf{y}_{NLOS} and \mathbf{v}_{path} . The encoder and decoder are then jointly optimized to maximize an approximation of the log-likelihood called evidence lower bound (ELBO); see [36] for details.

In our case, the encoder and decoder are embodied by fully connected NNs configured as per Table I. Since the latent vector \mathbf{z}_{NLOS} is realized as a 20-dimensional Gaussian vector, the decoder accepts the 20-dimensional Gaussian vector plus

the five-dimensional transformed vector in (8) and yields the 120+120 means and variances. Conversely, the encoder is fed the transformed vector in (8) and a 120-dimensional data input and produces means and variances for the 20-dimensional latent vector.

3) *NLOS transformation*: As advanced, the generated vector \mathbf{y}_{NLOS} is a transformed version of the path parameters, the reason being that those parameters are heterogeneous: they include path losses, angles, and delays. To put them on an equal footing, they are transformed as follows:

- The path losses are converted to dB-scale path gains and the minimum value for such gain found in the dataset is subtracted. The resulting excess path gains are then scaled by a min-max scaler mapping to the interval [0,1]; a value of zero corresponds to no path.
- The angles are rotated relative to the LOS angle, and then scaled such that 180° corresponds to a unit value.
- The LOS delay is subtracted from the rest of delays, and the resulting excess delays are scaled by a min-max scaler mapping to the interval [0,1].

The above transformation ensures that all values are in a similar range and referenced to the LOS path. The min-max scalers for the path losses and delays are fit to the training data, and we note that the mapping of angles and delays relative to the LOS path can be effected even if such LOS path is blocked.

Once \mathbf{y}_{NLOS} has been generated, the transformation must be undone to obtain the NLOS path parameters, \mathbf{x}_{NLOS} .

4) *Addition of the LOS path*: For the LOS path, when it exists, the delay and angles of departure and arrival can be computed from sheer geometry while its loss can be computed from Friis' law [48]. The final step is the addition, when it exists, of such LOS path to \mathbf{x}_{NLOS} , which renders the full collection of path parameters, \mathbf{x} .

IV. RAY TRACING DATA AT 28 GHZ

Experimental data on UAV channels has been limited, particularly in the mmWave bands [18], [19], [50]–[52]. In this work, we employ a powerful ray tracing package, Wireless InSite by Remcom [40], which was also used in [41], [45].

To generate datasets, we consider four city sections having varying sizes and distinct types of terrain, buildings, and foliage. Fig. 2 shows 3D representations of these four city sections. The number of deployed transmitters (UAVs) and receivers (gNBs) is detailed in Table II for each of the cities.

It is standard practice to differentiate channel models across environments, e.g., the 3GPP mmWave model [17] provides separate parameter distributions for environments such as *urban macro* and *urban micro*. In a data-based approach, environment-specific models can be created by partitioning the training data. In our case, we delineate these two environments:

- *Tokyo-Beijing*: A first environment is based on the data from the Tokyo and Beijing sections, featuring some high-rise buildings while including wide open areas and parks.
- *London-Moscow*: A second environment consist of the data from the London and Moscow sections, where there is an abundance of low-rise buildings (of different densities).

TABLE II: City sections and deployment parameters

	Tokyo, Japan	Beijing, China	London, UK	Moscow, Russia
Environment size (m^2)	1420×1440	1650×1440	1500×1480	1440×1380
Number of UAVs	140	120	120	160
Number of terrestrial gNBs	220	180	122	200
Number of aerial gNBs	200	120	93	160

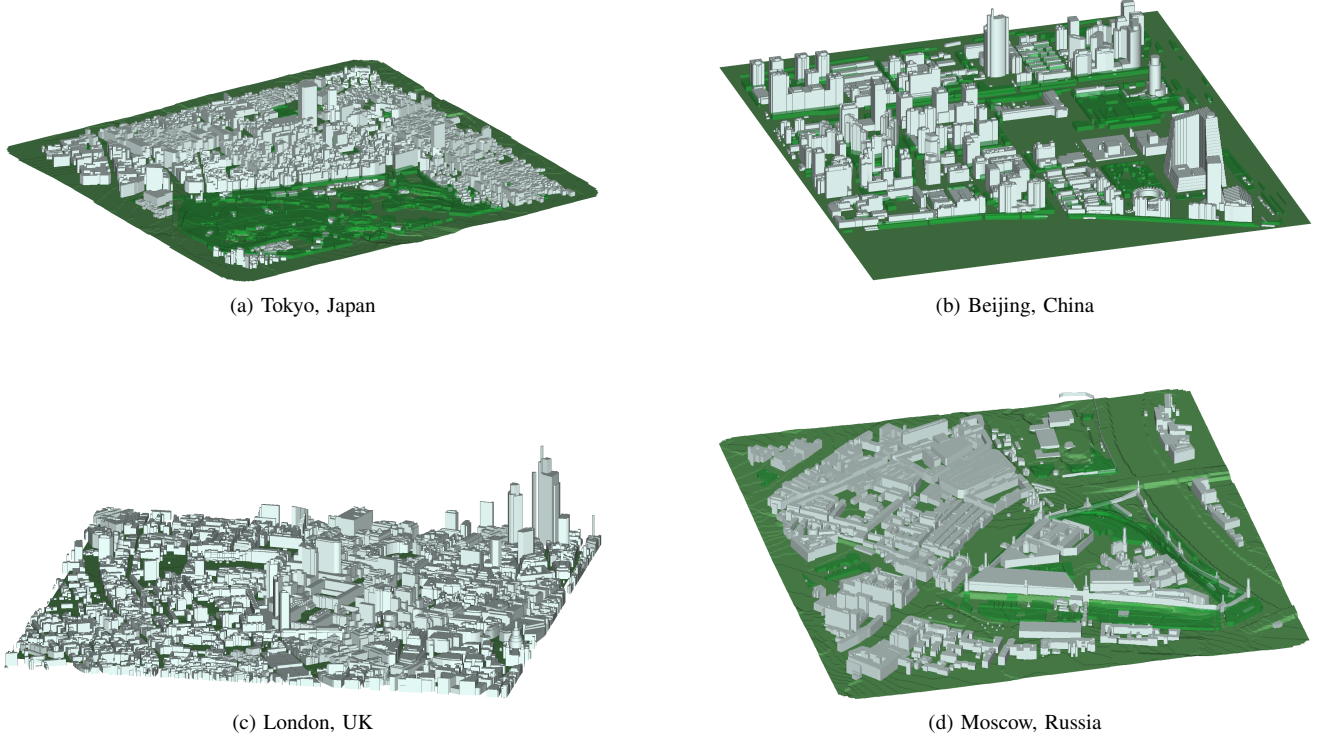


Fig. 2: 3D representations of the four considered city sections: (a) Tokyo, (b) Beijing, (c) London, and (d) Moscow.

For our data production, two distinct types of gNBs are manually placed:

- *Terrestrial gNBs*: These gNBs are placed on streets at an approximate height of 2 m, emulating typical locations for 5G microcells designed to serve ground users. We are interested in modeling the air-to-ground channels seen by gNBs at such locations, both to verify whether terrestrial cells can serve UAVs and to understand the interference between UAV and terrestrial transmissions therein.
- *Aerial gNBs*: These gNBs are located on rooftops, typically 30 m above street level, meant to provide additional coverage to UAVs, particularly at high altitudes.

Transmitting UAVs, for their part, are placed at different (x, y) locations in each city section at one of four possible altitudes: 30 m, 60 m, 90 m and 120 m.

In total, 94800 UAV-gNB links are created for the Tokyo-Beijing environment while 83400 links are put in place for the London-Moscow environment. The Wireless InSite tool is then run to simulate the channel on every link, producing the path parameters \mathbf{x} for each link. All simulations are conducted at 28 GHz. The maximum number of reflections is set to six and the maximum number of diffractions is set to one, with

both ground and wall surfaces taken to be made of concrete with a permittivity of 5.31 F/m. The simulator provides the directions of arrival and departure, as well as the path losses for each link.

The datasets thus gathered are utilized to train the model detailed in Sec. III.

V. MODELING RESULTS

This section describes various features of the learned models, and their ability to capture interesting wireless phenomena. We also seek to evaluate the generalization ability of the models, meaning their ability to accurately describe the channel behavior in locations other than those in the training. As mentioned in the introduction, this ability is a highly desirable attribute, and hence we test extensively.

The links available for each environment are split, 75% for training and 25% for testing. Models are then trained separately for each environment, which enables assessing the generalization ability in these two senses:

- *Intra-environment*: The model trained on the Tokyo-Beijing (respectively London-Moscow) dataset is evaluated on the Tokyo-Beijing (respectively London-Moscow)

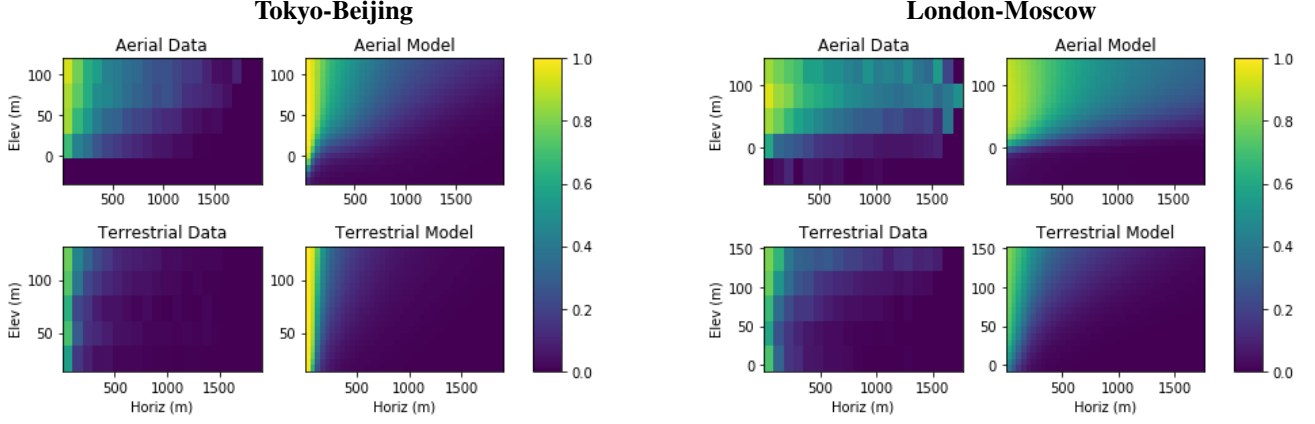


Fig. 3: Conditional probability of a LOS link as a function of horizontal and vertical distance to the gNB for terrestrial and aerial types and for the two environments. For each environment, the left-hand-side column is the empirical distribution on the test data and the right-hand-side column is the probability forecast by the trained link-state predictor.

test data. This appraises the ability of each model to generalize to links in their respective environments, but at new locations not seen during training.

- *Inter-environment:* The model trained on the Tokyo-Beijing dataset is evaluated on the London-Moscow test data, and vice versa. This serves to examine each model's ability to generalize to links in the other environment.

All the implementations are based on Tensorflow 2.2; the code, datasets, and pre-trained models can be found in [47].

A. LOS Probability

To illustrate the functioning of the link state predictor, Fig. 3 shows the conditional probability of the link being in the LOS state given its horizontal and vertical distances for the Tokyo-Beijing and London-Moscow environments. For each environment, the bottom subfigures present the probability corresponding to terrestrial gNBs and the top subfigures present the probability corresponding to aerial gNBs, while the left-hand-side columns show the actual values on the test data and the right-hand-side columns show the probability at the output of the trained link-state predictor.

The link-state predictor is seen to match the basic trends of the empirical distribution, and to reflect the very different behaviors of terrestrial and aerial gNBs. In particular, aerial gNBs can provide high probabilities of LOS coverage at long horizontal distances provided the UAV is high enough. In contrast, terrestrial gNBs are much more limited in terms of horizontal coverage.

We also observe an interesting difference between the Tokyo-Beijing and the London-Moscow environments: the LOS probability is much higher in London-Moscow at greater distances, both for terrestrial and aerial gNBs. This is consistent with the relatively smaller building heights therein. We will see how this has a significant impact in other features such as the pathloss.

B. Path Loss: Intra-Environment Evaluation

We now turn to evaluating the accuracy of the rest of the parameters. Fundamentally, we want to measure how close

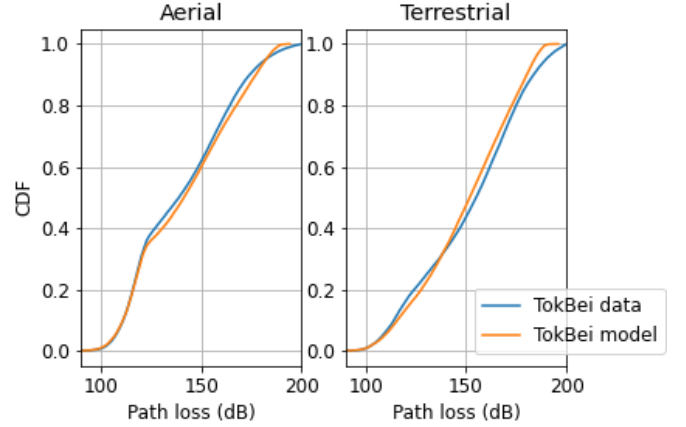


Fig. 4: Intra-environment prediction of omnidirectional path losses: “TokBei data” is the CDF for links in the test dataset of the Tokyo-Beijing environment; “TokBei model” is the CDF of values generated by the model trained on the same Tokyo-Beijing dataset with the same link conditions as the test data. In both cases, the path loss is only plotted for the links in LOS and NLOS states, with NoLink cases excluded.

the distribution of the trained generative model in (3) is to the observed conditional distribution of the test data itself. To this end, let $(\mathbf{u}_i, \mathbf{x}_i)$, $i = 1, \dots, N_{ts}$ be the test samples, each containing a link condition, \mathbf{u}_i , and its corresponding path parameters, \mathbf{x}_i . To evaluate how closely the learned model fits this test data, for each sample we can compute some statistic $v_i = \phi(\mathbf{u}_i, \mathbf{x}_i)$ that is of relevance. As an example, we compute the path loss experienced by UAVs and gNBs equipped with omnidirectional antennas; directional metrics are entertained later in the paper.

Using the same conditions \mathbf{u}_i in the test data, we generate a sample $\mathbf{x}_i^{\text{rnd}} = g(\mathbf{u}_i, \mathbf{z}_i)$ from the trained generative model and a random \mathbf{z}_i . We can then compute $v_i^{\text{rnd}} = \phi(\mathbf{u}_i, \mathbf{x}_i^{\text{rnd}})$ and compare the CDFs of v_i^{rnd} and v_i .

We first evaluate the intra-environment accuracy of the omni-directional path loss predictions. Fig. 4 shows the empirical CDF of path losses for the Tokyo-Beijing test data

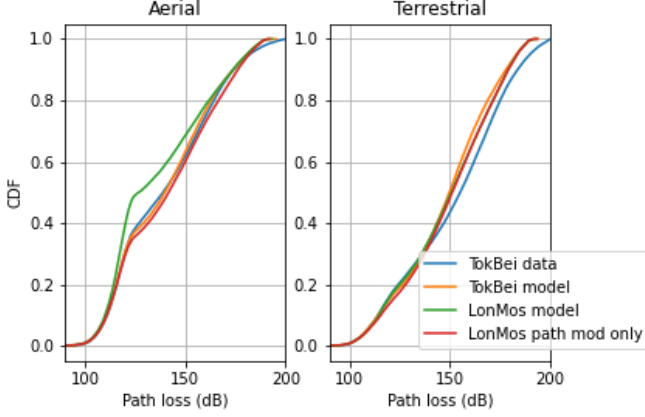


Fig. 5: Inter-environment prediction of omnidirectional path losses: “TokBei data” and “TokBei model” are the CDFs from Fig. 4; “LonMos model” is the CDF of values generated by the model trained on the London-Moscow dataset; “LonMos path mod only” is the CDF when using the path generator trained from the London-Moscow data, but with the actual link state (LOS, NLOS and NoLink) as opposed to the model-generated one.

alongside the CDF of path losses generated by the trained model using the same condition values as the test data. An excellent match is observed for both terrestrial and aerial gNBs. In particular, the trained generative model is able to capture the dual-slope nature of the CDF arising from the mixture of LOS/NLOS links. Similar results were observed in the London-Moscow environment.

C. Path Loss: Inter-Environment Evaluation

Fig. 5 reproduces again, as baselines, the CDF of omnidirectional path losses for the test data in the Tokyo-Beijing dataset, and from the model trained on that same environment. As observed in Fig. 4, these CDFs match well, indicating that the modeled trained in a given environment can predict the behavior of new links in that same environment.

The figure also presents the CDF of path losses generated by the model trained on the London-Moscow dataset, but with the link conditions from the Tokyo-Beijing test dataset. Interestingly, as far as terrestrial gNBs are concerned, the model trained on the London-Moscow environment matches well the Tokyo-Beijing environment, suggesting that the distribution of the link parameters—conditioned on the gNB type and distance—are similar for the two environments. For the aerial gNBs, however, there is a noticeable disagreement. To determine the source of this disagreement, Fig. 5 also depicts the CDF when using London-Moscow-trained model for the path generator network, but the true link state (LOS, NLOS or NoLink) rather than the model-generated one. In this case, the path generative network trained on the London-Moscow data matches the distribution of the paths seen in the Beijing-Tokyo environment.

We thus see how the proposed methodology enables assessing the inter-environmental generalizability of models. In the case at hand specifically, we see that the generalizability depends critically on the gNB type and on the parts of the

models we consider. For terrestrial gNBs, a model trained in London-Moscow can predict both the link state (LOS vs. NLOS) and the conditional distribution of the path losses given the link state in the Tokyo-Beijing environment. For aerial gNBs, however, the model trained in London-Moscow does *not* predict the link state well (it over-predicts the probability of LOS). This observation is consistent with the results in Section V-A. However, correcting for the link state, the London-Moscow-trained model can predict the path losses in Tokyo-Beijing.

Of course, based on the results of these four cities, we cannot make a general statement about the generalizability of channel models across different urban environments. More cities would need to be tested. Our point is that the methodology presented here provides a clear path for assessing generalizability across different environments.

D. Angular Distribution

We now turn to the path angles. Fig. 6 plots the distribution of those angles conditioned on the distance between the UAV and gNB. The conditional distribution is computed over all the paths within 30 dB of the strongest path within each link for all the links in the test dataset. For the sake of readability, the terrestrial and aerial gNBs are combined and the total link distance (horizontal and elevation) is considered. Nevertheless, respective plots for the aerial and terrestrial gNBs, or plots to separately observe the effects of elevation and horizontal distance, could also be put together from the model.

Each row in Fig. 6 shows the conditional distribution of one of the four angles, $\phi_k^{\text{rx}}, \theta_k^{\text{rx}}, \phi_k^{\text{tx}}, \theta_k^{\text{tx}}$, relative to the LOS direction (even when the LOS path does not exist, meaning it is blocked). For each environment, the left-hand-side column is the conditional distribution of the angles for the test data whereas the right-hand-side column is the conditional distribution of angles generated by the learned model.

The model matches very well the general trends in the angular distribution. In particular, it captures an important phenomenon: for all distances and angles, the NLOS paths tend to be angularly close to the LOS direction. Moreover, the angular spread decreases—particularly at the gNB side—as the UAV and gNB are further apart. This behavior makes intuitive sense in that, as the UAV pulls away from the gNB, there is less local scattering to create angular dispersion.

It can also be observed that there is much greater scattering at the gNB side (the angles of arrival). This is due to the fact that, in many test locations, the UAV is elevated with minimal local scattering.

E. SNR Predictions

We finalize with a demonstration of a simple application enabled by the generative model. Specifically, we compute the predicted uplink (UAV to gNB) SNR as a function of the UAV position in the single-cell scenario described in Table III. The uplink SNR is of particular interest since this is usually the power-limited direction. A gNB is located at $(0, 0, h)$ with $h = 2$ m and $h = 30$ m in the terrestrial and aerial cases, respectively. In the terrestrial case, the gNB is modeled as

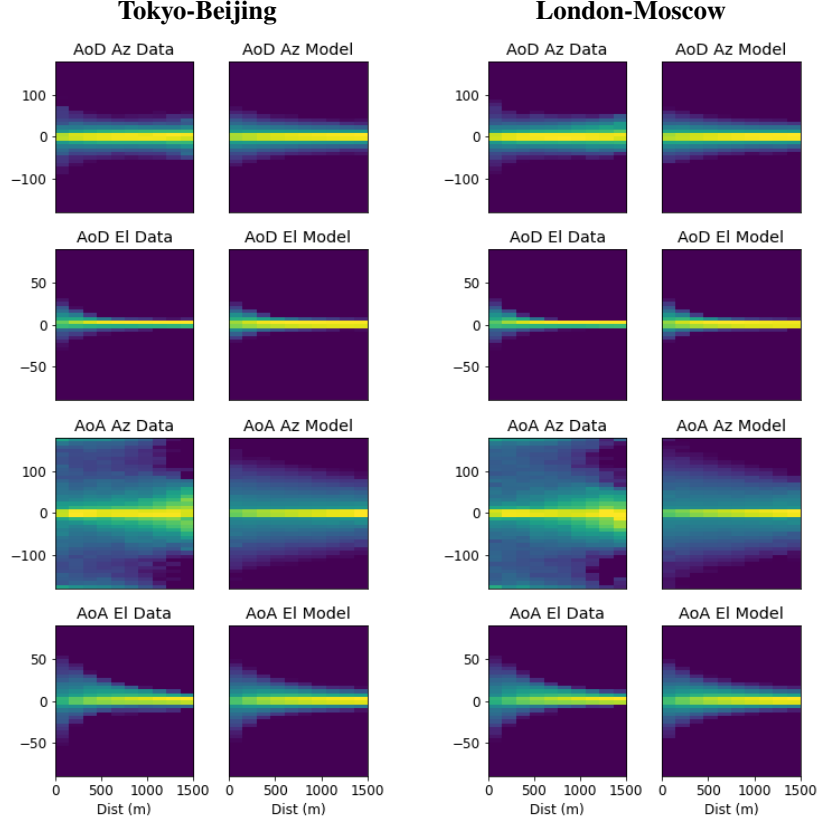


Fig. 6: Conditional distribution of the angles of the paths in each link relative to the LOS direction for the two environments. Only paths within 30 dB of the strongest path are included. Each row represents one of the four angles ϕ_k^{rx} , θ_k^{rx} , ϕ_k^{tx} , θ_k^{tx} . The left-hand-side column is the empirical condition distribution on the test data, the right-hand-side column is the distribution from the learned model.

TABLE III: Uplink single-cell simulation parameters.

Item	Value
Spectrum	Carrier frequency: 28 GHz Bandwidth: 400 MHz (4×100 MHz aggregation)
gNB height	Terrestrial: 2 m; Aerial: 30 m
Array size	UAV: $N_{UAV} = 16$ (4×4 UPA) gNB: $N_{gNB} = 64$ (8×8 UPA)
Antenna spacing	Half-wavelength
Array vertical angle	UAV: $180^\circ \searrow$ lower hemisphere coverage [53] Terrestrial gNB: $100^\circ \searrow$ ground coverage, 3 sectors Aerial gNB: $0^\circ \nearrow$ upper hemisphere coverage
Transmit power	UAV: 23 dBm
Losses	6 dB including noise figures [54], [55]

three-way sectorized with half-power beamwidth of 90° per sector; the arrays in each sector have a 10° downtilt, as customary to serve ground users, hence the connections to UAVs must be through sidelobes or reflected paths [12], [56]. In the aerial case, the gNB is single-sectorized with an upward-facing array intended for aerial coverage.

The UAV, which features a single array at its bottom, designed for lower-hemisphere coverage [53], is at a position $(x, 0, z)$ with $x \in [0, 500]$ m and $z \in [0, 130]$ m. For each UAV position and gNB type (aerial or terrestrial), 100 channels realizations are generated by the model. We apply a model learned from the Tokyo-Beijing data, yet a similar plot could be generated from the London-Moscow dataset as well.

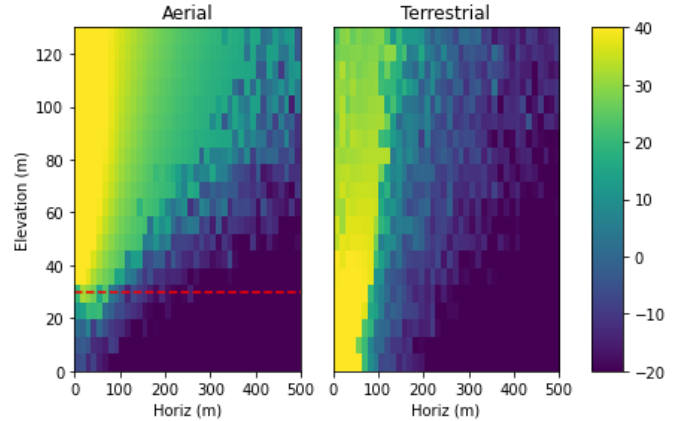


Fig. 7: Median SNR predicted by the model as a function of the horizontal and elevation position of the UAV for the Tokyo-Beijing environment. Details are provided in Table III. The red dotted line indicates the height of the aerial gNB.

From the channel paths and the link budget values in Table III, which are consistent with current 28 GHz 5G deployments [53], the local-average wideband SNR is computed. Fig. 7 plots the median SNR.

The experiment shows how SNR predictions can be produced from the model and the array specifics. The aerial gNBs provide much greater coverage at large horizontal distances,

yet terrestrial gNBs can provide solid coverage when the horizontal distance is small (less than 100 m). This coverage from terrestrial gNBs is rather surprising: complying with the 3GPP model [17], terrestrial gNBs have downtilted antennas with a 30 dB front-to-back gain, precluding connectivity from direct vertical paths. However, the learned model captures local scattering from neighboring buildings within the antenna beamwidth, and the simulations show that these paths do enable coverage.

VI. CONCLUSION

Generative NNs are a fitting engine for statistical channel modeling in complex settings such as those encountered in mmWave UAV communication. Provided that abundant data is available, generative NNs are perfectly equipped to learn intricate probabilistic relationships and then produce parameters distributed accordingly. The only assumption is the choice of the parameters themselves, which can rest on basic principles of radio propagation.

The proposed generative model, publicly available [47], has been shown to learn effectively and it can therefore be calibrated for any desired operating frequency, type of deployment, and environment, for which representative data is available. Likewise, the model can capture any dependence present in the data. In current standard-defined aerial channels, for instance, the distributions from which the angles of the multipath components are drawn do not depend on the distance; in contrast, and as intuition would have it, our model indicates a progressive narrowing of these distributions over distance.

In closing, we recall that, while driven by ray-tracing data the model has proved its ability to learn and already made interesting predictions, the ultimate objective is to drive it with empirical data. For this purpose, a measurement collection campaign is underway.

REFERENCES

- [1] W. Xia, S. Rangan, M. Mezzavilla, A. Lozano, G. Geraci, V. Semkin, and G. Loianno, "Millimeter wave channel modeling via generative neural networks," to appear in *Proc. IEEE Globecom Workshops*. Available as *arXiv:2008.11006*, Aug. 2020.
- [2] 3GPP Technical Specification 22.125, "Technical specification group services and system aspects; unmanned aerial system (UAS) support in 3GPP; Stage 1; Release 17," Dec. 2019.
- [3] 3GPP Technical Specification 22.829, "Technical specification group services and system aspects; enhancements for unmanned aerial vehicles; Stage 1; Release 17," Sep. 2019.
- [4] G. Geraci, A. Garcia-Rodriguez, and X. Lin, "Preparing the ground for drone communications," in *IEEE ComSoc Technology News*, June 2019.
- [5] A. Fotouhi, H. Qiang, M. Ding, M. Hassan, L. Galati-Giordano, A. Garcia-Rodriguez, and J. Yuan, "Survey on UAV cellular communications: Practical aspects, standardization advancements, regulation, and security challenges," *IEEE Commun. Surveys Tuts.*, vol. 21, no. 4, pp. 3417–3442, 2019.
- [6] M. Mozaffari, W. Saad, M. Bennis, Y. Nam, and M. Debbah, "A tutorial on UAVs for wireless networks: Applications, challenges, and open problems," *IEEE Commun. Surveys Tuts.*, vol. 21, no. 3, pp. 2334–2360, third quarter 2019.
- [7] A. Garcia-Rodriguez, G. Geraci, D. López-Pérez, L. Galati Giordano, M. Ding, and E. Björnson, "The essential guide to realizing 5G-connected UAVs with massive MIMO," *IEEE Commun. Mag.*, pp. 2–8, 2019.
- [8] X. Lin, R. Wren, S. Euler, A. Sadam, H. Mänttinen, S. Muruganathan, S. Gao, Y. E. Wang, J. Kauppi, Z. Zou, and V. Yajnanarayana, "Mobile network-connected drones: Field trials, simulations, and design insights," *IEEE Veh. Tech. Mag.*, vol. 14, no. 3, pp. 115–125, 2019.
- [9] Y. Zeng, J. Lyu, and R. Zhang, "Cellular-connected UAV: Potentials, challenges and promising technologies," *IEEE Wireless Commun. Mag.*, vol. 26, no. 1, pp. 120–127, Feb. 2019.
- [10] M. M. Azari, F. Rosas, and S. Pollin, "Cellular connectivity for UAVs: Network modeling, performance analysis and design guidelines," *IEEE Trans. Wireless Commun.*, vol. 18, no. 7, pp. 3366–3381, July 2019.
- [11] H. C. Nguyen, R. Amorim, J. Wigard, I. Z. Kovács, T. B. Sørensen, and P. Mogensen, "How to ensure reliable connectivity for aerial vehicles over cellular networks," *IEEE Access*, vol. 6, pp. 12 304–12 317, Feb. 2018.
- [12] 3GPP Technical Report 36.777, "Technical specification group radio access network; Study on enhanced LTE support for aerial vehicles (Release 15)," Dec. 2017.
- [13] M. Polese, L. Bertizzolo, L. Bonati, A. Gosain, and T. Melodia, "An Experimental mmWave Channel Model for UAV-to-UAV Communications," in *Accepted at the 4th ACM Workshop on Millimeter-wave Networks and Sensing Systems (mmNets'20)*, 2020.
- [14] S. Rangan, T. S. Rappaport, and E. Erkip, "Millimeter-wave cellular wireless networks: Potentials and challenges," *Proceedings of the IEEE*, vol. 102, no. 3, pp. 366–385, 2014.
- [15] T. S. Rappaport, R. W. Heath Jr., R. C. Daniels, and J. N. Murdock, *Millimeter Wave Wireless Communications*. Pearson Education, 2014.
- [16] S. Wu, C.-X. Wang, M. Alwakeel, X. You *et al.*, "A general 3-D non-stationary 5G wireless channel model," *IEEE Trans. Commun.*, vol. 66, no. 7, pp. 3065–3078, 2017.
- [17] 3GPP Technical Report 38.901, "Study on channel model for frequencies from 0.5 to 100 GHz (Release 16)," Dec. 2019.
- [18] W. Khawaja, I. Guvenc, D. W. Matolak, U. Fiebig, and N. Schneckenburger, "A survey of air-to-ground propagation channel modeling for unmanned aerial vehicles," *IEEE Commun. Surveys & Tutorials*, vol. 21, no. 3, pp. 2361–2391, 2019.
- [19] R. Amorim, H. Nguyen, P. Mogensen, I. Z. Kovács, J. Wigard, and T. B. Sørensen, "Radio channel modeling for UAV communication over cellular networks," *IEEE Wireless Commun. Letters*, vol. 6, no. 4, pp. 514–517, 2017.
- [20] L. Cheng, Q. Zhu, C. Wang, W. Zhong, B. Hua, and S. Jiang, "Modeling and simulation for UAV air-to-ground mmWave channels," in *European Conf. Antennas and Propagation (EuCAP'20)*, 2020, pp. 1–5.
- [21] K. Stocker, B. Gschwendtner, and F. Landstorfer, "Neural network approach to prediction of terrestrial wave propagation for mobile radio," in *IEEE Proceedings H (Microwaves, Antennas and Propagation)*, vol. 140, no. 4, 1993, pp. 315–320.
- [22] P.-R. Chang and W.-H. Yang, "Environment-adaptation mobile radio propagation prediction using radial basis function neural networks," *IEEE Trans. Veh. Techn.*, vol. 46, no. 1, pp. 155–160, 1997.
- [23] L. Bai, C.-X. Wang, J. Huang, Q. Xu, Y. Yang, G. Goussetis, J. Sun, and W. Zhang, "Predicting wireless mmWave massive MIMO channel characteristics using machine learning algorithms," *Wireless Commun. and Mobile Computing*, 2018.
- [24] J. Huang, C.-X. Wang, L. Bai, J. Sun, Y. Yang, J. Li, O. Tirkkonen, and M. Zhou, "A big data enabled channel model for 5G wireless communication systems," *IEEE Trans. Big Data*, 2018.
- [25] X. Zhao, F. Du, S. Geng, Z. Fu, Z. Wang, Y. Zhang, Z. Zhou, L. Zhang, and L. Yang, "Playback of 5G and beyond measured MIMO channels by an ANN-based modeling and simulation framework," *IEEE J. Sel. Areas Commun.*, vol. 38, no. 9, pp. 1945–1954, 2020.
- [26] E. Ostlin, H.-J. Zepernick, and H. Suzuki, "Macrocell path-loss prediction using artificial neural networks," *IEEE Trans. Veh. Techn.*, vol. 59, no. 6, pp. 2735–2747, 2010.
- [27] E. Dall'Anese, S.-J. Kim, and G. Giannakis, "Channel gain map tracking via distributed kriging," *IEEE Trans. Veh. Techn.*, vol. 60, no. 3, pp. 1205–1211, 2011.
- [28] L. Azpilicueta, M. Rawat, K. Rawat, F. Ghannouchi, and F. Falcone, "A ray launching-neural network approach for radio wave propagation analysis in complex indoor environments," *IEEE Trans. Antennas Propag.*, vol. 62, no. 5, pp. 2777–2786, 2014.
- [29] M. Kasparick, R. Cavalcante, S. Valentin, S. Stańczak, and M. Yukawa, "Kernel-based adaptive online reconstruction of coverage maps with side information," *IEEE Trans. Veh. Techn.*, vol. 65, no. 7, pp. 5461–5473, 2015.
- [30] G. Ferreira, L. Matos, and J. Silva, "Improvement of outdoor signal strength prediction in UHF band by artificial neural network," *IEEE Trans. Antennas Propag.*, vol. 64, no. 12, pp. 5404–5410, 2016.

- [31] D. Romero, S.-J. Kim, G. Giannakis, and R. López-Valcarce, "Learning power spectrum maps from quantized power measurements," *IEEE Trans. Signal Processing*, vol. 65, no. 10, pp. 2547–2560, 2017.
- [32] X. Ma, J. Zhang, Y. Zhang, and Z. Ma, "Data scheme-based wireless channel modeling method: motivation, principle and performance," *J. Commun. Inform. Netw.*, vol. 2, no. 3, pp. 41–51, 2017.
- [33] R. Nikbakht, A. Jonsson, and A. Lozano, "Dual-kernel online reconstruction of power maps," in *IEEE Global Commun. Conf. (GLOBECOM'18)*, 2018, pp. 1–5.
- [34] A. Radford, L. Metz, and S. Chintala, "Unsupervised representation learning with deep convolutional generative adversarial networks," *arXiv preprint arXiv:1511.06434*, 2015.
- [35] I. Goodfellow, J. Pouget-Abadie, M. Mirza, B. Xu, D. Warde-Farley, S. Ozair, A. Courville, and Y. Bengio, "Generative adversarial nets," in *Proc. Advances in neural information processing systems*, 2014, pp. 2672–2680.
- [36] C. Doersch, "Tutorial on variational autoencoders," *arXiv preprint arXiv:1606.05908*, 2016.
- [37] Y. Yang, Y. Li, W. Zhang, F. Qin, P. Zhu, and C. Wang, "Generative-adversarial-network-based wireless channel modeling: Challenges and opportunities," *IEEE Commun. Magazine*, vol. 57, no. 3, pp. 22–27, 2019.
- [38] T. J. O'Shea, T. Roy, and N. West, "Approximating the void: Learning stochastic channel models from observation with variational generative adversarial networks," in *Int'l Conf. Computing, Netw. and Commun. (ICNC'19)*, 2019, pp. 681–686.
- [39] H. Ye, L. Liang, G. Y. Li, and B. Juang, "Deep learning-based end-to-end wireless communication systems with conditional GANs as unknown channels," *IEEE Trans. Wireless Commun.*, vol. 19, no. 5, pp. 3133–3143, 2020.
- [40] "Remcom," available on-line at <https://www.remcom.com/>.
- [41] A. Alkhateeb, "DeepMIMO: A generic deep learning dataset for millimeter wave and massive MIMO applications," in *Proc. of Information Theory and Applications Workshop (ITA)*, San Diego, CA, Feb 2019, pp. 1–8.
- [42] V. Degli-Esposti, F. Fuschini, E. M. Vitucci, M. Barbiroli, M. Zoli, L. Tian, X. Yin, D. A. Dupleich, R. Müller, C. Schneider *et al.*, "Ray-tracing-based mm-wave beamforming assessment," *IEEE Access*, vol. 2, pp. 1314–1325, 2014.
- [43] Z. Chen, H. Gao, D. Leenaerts, D. Milosevic, and P. Baltus, "A 29–37 GHz BiCMOS Low-Noise Amplifier with 28.5 dB Peak Gain and 3.1–4.1 dB NF," in *Proc. IEEE RFIC*, 2018, pp. 288–291.
- [44] A. Al-Hourani, S. Kandeepan, and A. Jamalipour, "Modeling air-to-ground path loss for low altitude platforms in urban environments," in *Proc. IEEE Globecom*, 2014, pp. 2898–2904.
- [45] Z. Yun and M. F. Iskander, "Ray tracing for radio propagation modeling: Principles and applications," *IEEE Access*, vol. 3, pp. 1089–1100, 2015.
- [46] W. Khawaja, O. Ozdemir, and I. Guvenc, "UAV Air-to-Ground Channel Characterization for mmWave Systems," in *Proc. IEEE VTC-Fall*, 2017.
- [47] F. Fuschini, S. Häfner, M. Zoli, R. Müller, E. Vitucci, D. Dupleich, M. Barbiroli, J. Luo, E. Schulz, V. Degli-Esposti *et al.*, "Analysis of in-room mm-wave propagation: Directional channel measurements and ray tracing simulations," *Journal of Infrared, Millimeter, and Terahertz Waves*, vol. 38, no. 6, pp. 727–744, 2017.
- [48] "mmWave channel modeling git hub repository," available on-line at <https://github.com/nyu-wireless/mmwhchanmod>.
- [49] R. W. Heath Jr. and A. Lozano, *Foundations of MIMO Communication*. Cambridge University Press, 2018.
- [50] M. R. Akdeniz, Y. Liu, M. K. Samimi, S. Sun, S. Rangan, T. S. Rappaport, and E. Erkip, "Millimeter wave channel modeling and cellular capacity evaluation," *IEEE journal on selected areas in communications*, vol. 32, no. 6, pp. 1164–1179, 2014.
- [51] A. A. Khuwaja, Y. Chen, N. Zhao, M. S. Alouini, and P. Dobbins, "A survey of channel modeling for UAV communications," *IEEE Commun. Surveys & Tutorials*, vol. 20, no. 4, pp. 2804–2821, 2018.
- [52] R. Amorim, P. Mogensen, T. Sorensen, I. Z. Kovács, and J. Wigard, "Pathloss measurements and modeling for UAVs connected to cellular networks," in *IEEE Veh. Techn. Conf. (VTC'17 Spring)*, 2017, pp. 1–6.
- [53] R. Amorim, H. Nguyen, J. Wigard, I. Z. Kovács, T. B. Sorensen, and P. Mogensen, "LTE radio measurements above urban rooftops for aerial communications," in *IEEE Wireless Commun. Netw. Conf. (WCNC'18)*, 2018, pp. 1–6.
- [54] W. Xia, M. Polese, M. Mezzavilla, G. Loianno, S. Rangan, and M. Zorzi, "Millimeter Wave Remote UAV Control and Communications for Public Safety Scenarios," in *16th Annual IEEE International Conference on Sensing, Communication, and Networking (SECON)*, 2019.
- [55] R. Garg and A. S. Natarajan, "A 28-GHz Low-Power Phased-Array Receiver Front-End With 360° RTPS Phase Shift Range," *IEEE Trans. Microw. Theory Tech.*, vol. 65, no. 11, pp. 4703–4714, 2017.
- [56] G. Geraci, A. Garcia Rodriguez, L. Galati Giordano, D. López-Pérez, and E. Björnson, "Understanding UAV cellular communications: From existing networks to massive MIMO," *IEEE Access*, vol. 6, Nov. 2018.